Contribution from the Department of Chemistry and Laboratory of Molecular Structure and Bonding, Texas A&M University, College Station, Texas 77843, and Department of Chemistry, Michigan State University, East Lansing, Michigan 48824

Further Investigation of Molecular, Magnetic, and Electronic Structures of 2-Hydroxypyridinate Complexes of Diruthenium(II)

F. Albert Cotton,*[1a] Tong Ren,[1a] and Judith L. Eglin[1b]

Received October 26, 1990

Another new $Ru_2(xhp)_4$ type compound, $Ru_2(fhp)_4(thf)$ (fhp^- = 6-fluoro-2-hydroxypyridinate), has been prepared from $Ru_2(O_2CCH_3)_4$ and characterized by X-ray crystallography and magnetic susceptibility measurements from ca. 5 to ca. 300 K. Dark brown $Ru_2(fhp)_4(thf)$ crystallizes in space group $P2_12_12_1$ with a = 16.392 (4) Å, b = 17.161 (5) Å, c = 9.148 (2) Å, V = 2573 (1) Å^3, and Z = 4. The structure determined has Ru–Ru = 2.274 (1) Å and a polar ligand arrangement placing all like atoms (i.e., N's or O's) on the same metal centers. The magnetic behavior is identical with those previously described for three other 2-hydroxypyridinate complexes and is thus consistent with a ground state derived from a $(\pi^*)^2(\delta^*)^2$ configuration, which is also required by the Ru–Ru bond length. A $(\pi^*)^3(\delta^*)$ configuration is explicitly excluded as a possible ground-state configuration for all carboxylate and hydroxypyridinate complexes of diruthenium(II) on the basis of an analysis that leads to a prediction of qualitatively different behavior of the effective magnetic moments as a function of temperature. SCF–Xα calculations provide quantitative support for the $(\pi^*)^2(\delta^*)^2$ configuration. A singlet–triplet Boltzmann distribution based on $(\pi^*)^4$ and $(\pi^*)^3(\delta^*)$ configurations also fails to have the type of temperature dependence in accord with experiment.

Introduction

The study of diruthenium complexes is a very active and controversial area in metal–metal bonding chemistry. Due to the d-electron-rich character of ruthenium, some interesting new features, as well as complexities, have emerged in the molecular electronic structures.[2] In the case of $Ru_2(LL)_4$, the most important class of diruthenium(II) complexes, the bonding question has been extensively discussed in recent years.[3-14]

For diruthenium(II) complexes, there are 12 valence d electrons from the metal cores. While eight of the electrons must be assigned to $(\sigma)^2(\pi)^4(\delta)^2$ without hesitation, the remaining four electrons can be assigned to one of three configurations, $(\pi^*)^4$, $(\pi^*)^3(\delta^*)$, or $(\pi^*)^2(\delta^*)^2$, depending on the relative order of the δ^* and the π^* energy levels. Without ambiguity, diruthenium(II,II) triazeno complexes,[11,12] $Ru_2(RNNNR)_4$, were assigned the $(\pi^*)^4$ configuration on the basis of their distinctive long Ru–Ru bond distances and room-temperature diamagnetism. The electronic configuration of $Ru_2(O_2CR)_4$ was initially assigned as $(\pi^*)^3(\delta^*)$,[5,8] but it was shown later that $(\pi^*)^2(\delta^*)^2$ is more consistent with the molecular structural data.[12] From the variable-temperature magnetic susceptibility studies,[6] it is found that the paramagnetism of $Ru_2(O_2CR)_4$ can be *best* explained by a zero-field-splitting (ZFS) model derived from the $(\pi^*)^2(\delta^*)^2$ configuration. In our previous work,[14] a series of complexes of the form $Ru_2(xhp)_4$ (xhp^- = 6-x-2-hydroxypyridinate anion, with x = Me, Cl, and Br) were characterized via X-ray diffraction and magnetic susceptibility studies. The electronic structures of these complexes were found to be very similar to those of the $Ru_2(O_2CR)_4$ molecules. A qualitative π-basicity model was also suggested to account for all of the electronic structures observed so far.

The fhp^- ligand is already known to behave somewhat differently from the other xhp^- ligands. Thus, it has been found that in the group 6 triad, the $M_2(fhp)_4$ molecules have a very different ligand arrangement from that in other $M_2(xhp)_4$ molecules.[15] Therefore, the synthesis and characterization of the fhp complex of diruthenium(II) were considered to be a nontrivial extension of our previous work. It was expected to provide an opportunity to observe how the electronic structure responds to a variation in the ligand arrangement.

Another point we address in this report is the following. The magnetic behaviors of both $Ru_2(O_2CR)_4$ and $Ru_2(xhp)_4$ were proven to be well explained by the properties of a $(\pi^*)^2(\delta^*)^2$ configuration, and the other possible paramagnetic configuration $(\pi^*)^3(\delta^*)$ was not expected, on qualitative grounds, to have the correct behavior. However, it had not been shown quantitatively to be inconsistent with the magnetic data. A quantitative, theoretical analysis remains desirable to remove any ambiguity.

This report also deals with a third point. The SCF–Xα method has been effectively used to explore the electronic structure of diruthenium species since the late 1970s. The ground-state configuration of $Ru_2(O_2CR)_4Cl$ was a riddle until Norman and co-workers assigned it as $(\pi^*)^2(\delta^*)$ on the basis of the results of a model Xα calculation.[8] Recently the Xα study of $Ru_2(RNNNR)_4$ type compounds has not only confirmed the $(\pi^*)^4$ configuration experimentally derived but has also allowed further quantitative analysis of the origin of the large δ^*–π^* gap.[20] It appeared logical to apply the same methodology to the study of hydroxypyridinate complexes of diruthenium(II).

(1) (a) Texas A&M University. (b) Michigan State University. Present address: Texas A&M University.
(2) (a) Cotton, F. A.; Walton, R. A. *Multiple Bonds Between Metal Atoms*; John Wiley & Sons: New York, 1982. (b) Cotton, F. A.; Walton, R. A. *Struct. Bonding* **1985**, *62*. (c) Cotton, F. A.; Walton, R. A. 2nd ed. of ref 2a.
(3) LL is an abbreviation for any three-atom, uninegative, bridging bidentate ligand; L is a monodentate axial ligand.
(4) (a) Berry, M.; Garner, C. D.; Hillier, I. H.; MacDowell, A. A.; Clegg, W. *Inorg. Chim. Acta* **1981**, *53*, L61. (b) Clegg, W. *Acta Crystallogr.* **1980**, *B36*, 3112.
(5) Lindsay, A. J.; Wilkinson, G.; Motevalli, Hursthouse, M. B. *J. Chem. Soc., Dalton Trans.* **1985**, 2321.
(6) Cotton, F. A.; Miskowski, V. M.; Zhong, B. *J. Am. Chem. Soc.* **1989**, *111*, 6177.
(7) Maldivi, P.; Giroud-Godquin, A.; Marchon, J.; Guillon, D.; Skoulios, A. *Chem. Phys. Lett.* **1989**, *157*, 552.
(8) Norman, J. G.; Renzoni, G. E.; Case, D. A. *J. Am. Chem. Soc.* **1979**, *101*, 5256.
(9) Clark, D. L.; Green, J. C.; Redfern, C. M. *J. Chem. Soc., Dalton Trans.* **1989**, 1037.
(10) Clark, D. L.; Green, J. C.; Redfern, C. M.; Quelch, G. E.; Hiller, I. H.; Guest, M. F. *Chem. Phys. Lett.* **1989**, *154*, 326.
(11) Lindsay, A. J.; Wilkinson, G.; Motevalli, M.; Hursthouse, M. B. *J. Chem. Soc., Dalton Trans.* **1987**, 2723.
(12) Cotton, F. A.; Matusz, M. *J. Am. Chem. Soc.* **1988**, *110*, 5761.
(13) Cotton, F. A.; Feng, X. *Inorg. Chem.* **1989**, *28*, 1180.
(14) Cotton, F. A.; Ren, T.; Eglin, J. L. *J. Am. Chem. Soc.* **1990**, *112*, 3439.
(15) Cotton, F. A.; Favello, L. R.; Han, S.; Wang, W. *Inorg. Chem.* **1983**, *22*, 4106.
(16) Bino, A.; Cotton, F. A.; Fanwick, P. E. *Inorg. Chem.* **1979**, *18*, 3558.
(17) Cotton, F. A.; Frentz, B. A.; Deganello, G.; Shaver, A. *J. Organomet. Chem.* **1973**, *50*, 227.
(18) North, A. C. T.; Phillips, D. C.; Mathews, F. S. *Acta Crystallogr., Sect. A: Cryst. Phys., Diffr., Theor. Gen. Crystallogr.* **1968**, *24A*, 351.
(19) (a) Slater, J. C. *Quantum Theory of Molecules and Solids*; McGraw-Hill: New York, 1974. (b) Johnson, K. H. *Adv. Quantum Chem.* **1973**, *7*, 143. (c) Connolly, J. W. D. In *Semiempirical Methods of Electronic Structure Calculation. Part A: Techniques*; Segal, G. A. Ed.; Plenum Press: New York, 1977.
(20) Norman, J. G., Jr. *Mol. Phys.* **1976**, *31*, 1191.

0020-1669/91/1330-2552$02.50/0

Experimental Section

Standard vacuum-line and Schlenk techniques were used to carry out the synthesis, and the compound was subsequently handled under an argon atmosphere. All the solvents used were of reagent grade or better from commercial sources and freshly distilled under N_2 over suitable drying reagents. The complex $Ru_2(OAc)_4$ was obtained by the standard method.[5] 6-Fluoro-2-pyridinol (Hfhp) was a generous gift from Dow Chemical Co.

$Ru_2(fhp)_4$. To prepare this compound, 0.23 g of Hfhp (2.0 mmol) was dissolved in 10 mL of THF and then this solution was cooled in a dry-ice bath. To this solution was added 1.3 mL of 1.6 M *n*-BuLi (in hexane). The solution was slowly warmed to room temperature and then transferred via cannula to a suspension of 0.22 g of $Ru_2(OAc)_4$ (0.5 mmol) in 10 mL of THF. The mixture was stirred at room temperature for 6 h to yield a dark green-brown solution with some colorless microcrystalline precipitate (LiOAc). After the LiOAc was removed by filtering the mixture through a fine frit, the clear solution was concentrated to ca. 10 mL and then layered with 20 mL of hexane. A large quantity of crystals of X-ray quality appeared within 1 week. These crystals were filtered out and dried under vacuum: yield ca. 0.215 g (53%). Both the molten reaction method and the substitution with the sodium salt of the ligand in MeOH used for the other hydroxypyridinate complexes[14] were also attempted with this ligand. The green solids so obtained failed to dissolve in any common organic solvents but dissolved and apparently reacted with pyridine (see Discussion). UV-vis (THF): 287 nm (ϵ 25 520 M^{-1} cm^{-1}); no characteristic peaks in the visible region. IR (cm^{-1}): 1601 m, 1283 s, 1213 s, 1180 m, 1114 w, 1090 m, 1051 s, 877 w, 818 s, 722 w, 591 m, 525 m, 478 m.

Physical Measurements. The UV-visible spectra were measured on a Cary 17D spectrometer at ambient temperature by using glass cells (900–400 nm) and quartz cells (400–220 nm). The IR spectra were recorded with an IBM IR/44 FT-IR instrument having a range 4000–400 cm^{-1}. The spectra of the solid samples were taken as Nujol mulls between CsI plates.

The variable-temperature magnetic susceptibility data were measured with an SHE 800 Series SQUID (superconducting quantum interference device) magnetometer at Michigan State University over a temperature range of 1.2 K to 300 K in applied fields of 5 kG (0.50 T) and 7 kG. The sample was loaded in a helium glovebox into a Kel-F bucket and then transferred to the instrument and loaded under a helium atmosphere. The sample was then rapidly cooled from room temperature to 5 K in zero field by loading it directly into the susceptometer and later also slowly cooled from 300 to 5 K in a field of 5 kG. No field dependence was observed or any difference in the susceptibility due to the two different thermal treatments of the sample.

X-ray Crystallography. A dark brown block was mounted under deoxygenated mineral oil in a Lindemann capillary. An orthorhombic cell was revealed via an initial indexing from 25 reflections with $16.5 \leq 2\theta \leq 21$. The *mmm* Laue symmetry was further confirmed by the oscillation photographs. From the systematic absences the space group was uniquely determined as $P2_12_12_1$ (No. 19). The data were collected on a Rigaku AFC5R diffractometer. The detailed discussion of the normal crystallographic procedures we followed are presented elsewhere.[16,17] The data set was corrected for decay, Lorentz, and polarization effects. Empirical absorption corrections based on the ψ-scan method was applied to the data.[18] The metal atoms and the atoms coordinated to them were located by the Patterson method (SHELX-86). Other non-hydrogen atoms were then introduced by an alternating series of difference Fourier maps and least-squares refinements using the SDP package. All of the non-hydrogen atoms were refined with anisotropic thermal parameters to low residuals. The composition was found to be $Ru_2(fhp)_4(thf)$ without any interstitial solvent. There was no attempt to determine the positions of the hydrogen atoms. The final figures of merit are collected in Table I.

Computational Procedures. The SCF–MS (multiple scattering)–Xα method[19] was used to calculate the electronic structures of several model complexes. The programs used were developed by Cook at Harvard University and Bursten and Stanley at Texas A&M University. All the calculations were carried out on either a VAXstation 2000 or a MicroVax computer in our own laboratory.

In all the calculations Norman's overlapping atomic sphere radii[20] were taken to be 88.5% of the atomic number radii. The outer sphere was made tangent to the outer atomic spheres. The α values of the atoms were obtained from Schwartz,[21] and the one for both intersphere and outer sphere was calculated as the valence-electron-weighted average of the atomic α. The starting molecular potentials were constructed as programmed by Cook and Case.[22] The SCF iteration was considered to be converged if the potential change was less than 10^{-3} Ry. For all the model molecules under consideration, the C–H, N–H, and O–H bond lengths were assumed to be 1.10, 1.00, and 0.95 Å, respectively. Only spin-restricted SCF was applied.

The fragment $HNC(H)O^-$ was used to mimic the xhp$^-$ anion. Both D_{2d} and C_{4v} geometries (see Figure 2) were considered, since they represented $Ru_2(mhp)_4$ and $Ru_2(fhp)_4(thf)$, respectively. For C_{4v} geometry, OH^- was chosen as a substitute for thf in order to preserve the 4-fold symmetry. Since this model molecule is a monoanion, a Watson sphere coincided with the outer sphere with a +1 charge was applied. A C_{4v} model without axial OH^- was also calculated for comparison. The geometrical parameters, determined via averaging the crystallographic bond distances and angles, are listed here: for D_{2d}, Ru–Ru = 2.235 Å, Ru–O = 2.049 Å, Ru–N = 2.086 Å, O–C = 1.293 Å, N–C = 1.365 Å, Ru–Ru–O = 92°, Ru–Ru–N = 89°, Ru–O–C = 119°, Ru–N–C = 119°; for C_{4v} (Ru_O and Ru_N are defined in Figure 2d), Ru_O–Ru_N = 2.274 Å, Ru_O–O = 2.042 Å, Ru_N–N = 2.087 Å, Ru_O–O_t = 2.275 Å, O–C = 1.292 Å, N–C = 1.366 Å, Ru_N–Ru_O–O = 92°, Ru_O–Ru_N–N = 89°, Ru_O–O–C = 121°, Ru_N–N–C = 119°. Due to the closeness of the π^* and δ^* energy levels, for all three calculations both $(\pi^*)^4$ and $(\pi^*)^2(\delta^*)^2$ configurations were put into the SCF iteration separately. For the D_{2d} model and the C_{4v} model without axial OH^-, the calculations converged on the $(\pi^*)^4$ configuration, while the calculation for the C_{4v} model with the axial OH^- converged on $(\pi^*)^2(\delta^*)^2$.

Table I. Crystallographic Data for $Ru_2(fhp)_4(thf)$

chem formula	$Ru_2F_4O_5N_4C_{24}H_{20}$
fw	722.6
space group	$P2_12_12_1$ (No. 19)
systematic abs	$h00$, $h = 2n$; $0k0$, $k = 2n$; $00l$, $l = 2n$
a, Å	16.392 (4)
b, Å	17.161 (5)
c, Å	9.148 (2)
V, Å^3	2573 (1)
Z	4
d_{calc}, g cm^{-3}	1.865
μ(Mo Kα), cm^{-1}	12.2
λ(Mo Kα), Å	0.710 73
T, °C	20 ± 1
max, min transm coeff	1.00, 0.960
R^a	0.046
R_w^b	0.066

$^a R = \sum||F_o| - |F_c||/\sum|F_o|$. $^b R_w = [\sum w(|F_o| - |F_c|)^2/\sum w|F_o|^2]^{1/2}$; $w = 1/\sigma^2(|F_o|)$.

Results and Discussions

As mentioned earlier, preparative procedures that were successful for other hydroxypyridinate complexes[14] only resulted in insoluble solids. When the substitution was carried out in THF with the lithium salt of the ligand (eq 1), however, a soluble

$$Ru_2(OAc)_4 + 4Lifhp \rightarrow Ru_2(fhp)_4(thf) + 4LiOAc\downarrow \quad (1)$$

product was obtained in a reasonable yield. This was used for the purposes of crystallization and spectroscopic studies. This procedure is also similar to those used in the synthesis of Cr and Mo analogues.[15]

The electronic spectrum of the complex is simple: no characteristic absorption occurs in the visible region, but there is a strong absorption occurring at 287 nm, which is most likely a ligand-localized transition.

This compound is crystallographically isomorphous with the previously known molybdenum and tungsten analogues.[15] Some important bond lengths and bond angles are listed in Table II. The molecular structure, as shown in Figure 1, has the four bridging 6-fluoro-2-hydroxypyridinate groups all aligned in the same direction along the metal–metal vector with all of the fluorine atoms staying at one end of the molecule, blocking the axial position. On the other axial position, a THF molecule is present. This polar C_{4v} arrangement is characteristic of the 6-fluoro-2-hydroxypyridinate ligand and has been observed in all of its tetrakis dimetallic complexes.[15,23–25] The Ru–Ru distance (2.274 (1) Å)

(21) Schwartz, K. *Phys. Rev.* **1972**, *5*, 2466.

(22) Cook, M.; Case, D. A. *Quantum Chemistry Program Exchange*. No. **465**, Indiana University.

(23) Cotton, F. A.; Matusz, M. *Polyhedron* **1987**, *6*, 1439.

(24) Cotton, F. A.; Han, S.; Wang, W. *Inorg. Chem.* **1984**, *23*, 4762.

Table II. Selected Bond Distances (Å) and Angles (deg) for $Ru_2(fhp)_4(thf)$[a]

Bond Distances			
Ru(1)-Ru(2)	2.274 (1)	Ru(2)-O(5)	2.275 (10)
Ru(1)-N(1)	2.094 (10)	O(1)-C(1)	1.27 (2)
Ru(1)-N(2)	2.095 (10)	O(2)-C(6)	1.287 (15)
Ru(1)-N(3)	2.069 (9)	O(3)-C(11)	1.303 (15)
Ru(1)-N(4)	2.090 (10)	O(4)-C(16)	1.309 (15)
Ru(2)-O(1)	2.046 (9)	N(1)-C(1)	1.40 (2)
Ru(2)-O(2)	2.046 (9)	N(2)-C(6)	1.36 (2)
Ru(2)-O(3)	2.039 (8)	N(3)-C(11)	1.354 (15)
Ru(2)-O(4)	2.037 (9)	N(4)-C(16)	1.35 (2)
Bond Angles			
Ru(2)-Ru(1)-N(1)	89.2 (3)	O(2)-Ru(2)-O(3)	90.5 (4)
Ru(2)-Ru(1)-N(2)	88.5 (3)	O(2)-Ru(2)-O(4)	176.0 (4)
Ru(2)-Ru(1)-N(3)	89.4 (3)	O(2)-Ru(2)-O(5)	87.9 (4)
Ru(2)-Ru(1)-N(4)	88.2 (3)	O(3)-Ru(2)-O(4)	89.8 (3)
N(1)-Ru(1)-N(2)	90.0 (4)	O(3)-Ru(2)-O(5)	86.9 (4)
N(1)-Ru(1)-N(3)	178.5 (4)	O(4)-Ru(2)-O(5)	88.1 (4)
N(1-)-Ru(1)-N(4)	90.6 (4)	Ru(2)-O(1)-C(1)	120.6 (9)
N(2)-Ru(1)-N(3)	90.5 (4)	Ru(2)-O(2)-C(6)	121.0 (8)
N(2)-Ru(1)-N(4)	176.6 (4)	Ru(2)-O(3)-C(11)	120.8 (8)
N(3)-Ru(1)-N(4)	88.9 (4)	Ru(2)-O(4)-C(16)	120.0 (8)
Ru(1)-Ru(2)-O(1)	92.1 (3)	Ru(1)-N(1)-C(1)	117.6 (8)
Ru(1)-Ru(2)-O(2)	91.6 (3)	Ru(1)-N(2)-C(6)	119.9 (8)
Ru(1)-Ru(2)-O(3)	91.0 (2)	Ru(1)-N(3)-C(11)	119.7 (8)
Ru(1)-Ru(2)-O(4)	92.3 (3)	Ru(1)-N(4)-C(16)	120.5 (8)
Ru(1)-Ru(2)-O(5)	177.8 (3)	O(1)-C(1)-N(1)	120 (1)
O(1)-Ru(2)-O(2)	90.2 (4)	O(2)-C(6)-N(2)	119 (1)
O(1)-Ru(2)-O(3)	176.8 (4)	O(3)-C(11)-N(3)	119 (1)
O(1)-Ru(2)-O(4)	89.3 (4)	O(4)-C(16)-N(4)	119 (1)
O(1)-Ru(2)-O(5)	90.1 (4)		

[a] Numbers in parentheses are estimated standard deviations in the least significant digits.

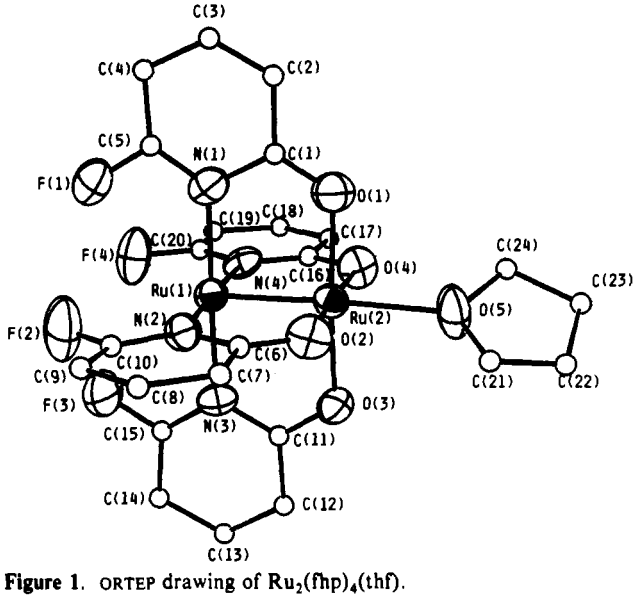

Figure 1. ORTEP drawing of $Ru_2(fhp)_4(thf)$.

is the longest among all the $Ru_2(xhp)_4$ complexes, and this cannot be attributed to the steric effect of the coordination mode of the fhp^- ligands, since the torsional angles O–Ru–Ru–N are all essentially zero (the determined torsional angles N(m)–Ru(1)–Ru(2)–O(m) with m = 1–4 are all virtually zero, namely, –0.76 (0.38), –0.52 (0.38), –0.47 (0.35), and 0.40 (0.36), respectively). The Ru(2)–O(5) distance (2.275 (10) Å) is substantially shorter than the corresponding ones in the Mo and W analogues (2.528 and 2.49 Å, respectively) and is the same as that for the Cr analogue (2.266 Å) as well as the Ru–O_{ax} distance in $[Ru_2(chp)_4]_2$ (2.290 and 2.265 Å). Since the covalent radii of Ru, Mo, and W are about the same, the shortness of this bond indicates a strong

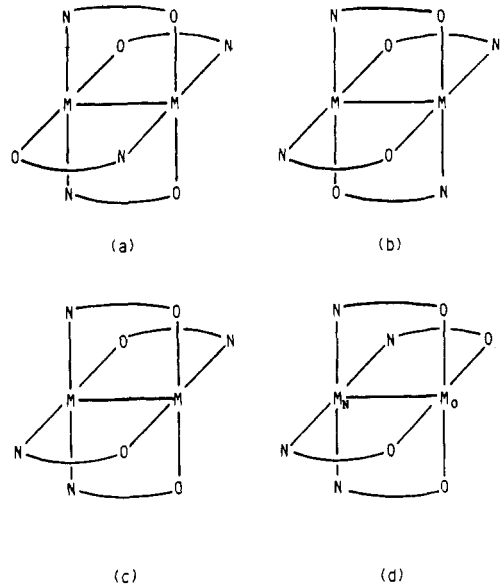

Figure 2. Four possible coordination modes for $M_2(xhp)_4$: (a) D_{2d}; (b) C_{2h}; (c) C_s; (d) C_{4v}.

interaction between Ru(2) and O(5), which would increase the electron density in both the σ^* and π^* orbitals on the metal core and results in a longer Ru–Ru distance. Also it is noteworthy that the Ru–Ru distance here is slightly shorter than that of $Ru_2(fhp)_4Cl$[25] (2.284 (1) Å), which obviously favors a $(\pi^*)^2(\delta^*)^2$ configuration.[14]

There are four possible coordination modes in a $M_2(xhp)_4$ molecule, as shown in Figure 2. Three of them were observed for $Ru_2(xhp)_4$ (D_{2d} and C_s geometries were found in an earlier study[14]), while the C_{2h} mode was observed in $Re_2(hp)_4Cl_2$[26] and possibly in $[Tc_2(hp)_4Cl]_n$.[27] The major factor determining the coordination mode is the size of the X atom (or group). The polar arrangements were found with smaller X like F and Cl, since the additional stability gained by axial coordination overcomes any additional steric hindrance in such arrangements. In contrast, one of the symmetrical arrangements (D_{2d} or C_{2h}) has to be taken by the ligands with larger X, like Me and Br, because only two of these large substituents can be accommodated on each end.

The measured molar magnetic susceptibility χ_M and the corresponding magnetic moment μ_{eff} ($\mu_{eff}^2 = 3k_BT\chi_M/N$, where k_B is the Boltzmann constant, N is Avogadro's number, and T is the temperature in Kelvin) for $Ru_2(fhp)_4(thf)$ were plotted versus the temperature, as shown in Figure 5. Although there is a rapidly rising tail (caused by an impurity) when T approaches closely to zero in the χ_M–T curves, a trend that μ_{eff} decreases as T decreases is very clear in the low-T region in the μ_{eff}–T curve. This indicates that the there is only weak paramagnetism at low temperature. However μ_{eff} at room temperature is about 2.3 μ_B (Bohr magneton), consistent with the presence of two unpaired electrons per molecule.

As mentioned earlier, there are three possible electronic configurations for the $Ru_2(LL)_4$ type complex, $(\pi^*)^4$, $(\pi^*)^3(\delta^*)$, and $(\pi^*)^2(\delta^*)^2$. While the first is excluded for $Ru_2(xhp)_4$, either of the other two could explain the presence of room-temperature paramagnetism. In the previous studies of the carboxylate complexes and the hydroxypyridinate complexes, it was shown that the magnetic properties could be *best* explained on the basis of a $(\pi^*)^2(\delta^*)^2$ model, while the behavior of $(\pi^*)^3(\delta^*)$ was uncertain. Here we present a more elaborate consideration of the temperature dependence of magnetic properties of the $(\pi^*)^3(\delta^*)$ configuration.

For the sake of the simplicity, the following discussion is couched in terms pertinent to D_{4h} point symmetry and ligand orbital mixing is ignored. The z axis is defined along the metal–metal vector.

(25) Charkravarty, A. R.; Cotton, F. A.; Schwotzer, W. *Polyhedron* **1986**, *5*, 1821.

(26) Cotton, F. A.; Gage, L. D. *Inorg. Chem.* **1979**, *18*, 1716.

(27) Cotton, F. A.; Fanwick, P. E.; Gage, L. D. *J. Am. Chem. Soc.* **1980**, *102*, 1570.

The π^* and δ^* orbitals can be expressed as

$$\delta^* = \frac{1}{\sqrt{2 - 2S_\delta^2}}[d_{xy}(1) - d_{xy}(2)] \quad (2a)$$

$$\pi_x^* = \frac{1}{\sqrt{2 + 2S_\pi^2}}[d_{xz}(1) + d_{xz}(2)] \quad (2b)$$

$$\pi_y^* = \frac{1}{\sqrt{2 + 2S_\pi^2}}[d_{yz}(1) + d_{yz}(2)] \quad (2c)$$

where $S_\pi = \langle xz(1)|xz(2)\rangle = \langle yz(1)|yz(2)\rangle$ and $S_\delta = \langle xy(1)|xy(2)\rangle$. The π^* and δ^* orbitals belong to the e_g and b_{2u} representations, respectively. On the basis of the electron-hole equivalence, we know that $(e_g)^3(b_{2u}) \Leftrightarrow (e_g)(b_{2u})$. Since $e_g \otimes b_{2u} = e_u$, the terms from $(\pi^*)^3(\delta^*)$ span the microstate space $^3E_u \oplus {}^1E_u$ with the triplet lying far below the singlet. There are spectral data for related cases to support the triplet $\ll$ singlet ordering.[28] For example, the energy difference between ^1E_u and ^3E_u was indirectly determined from well-resolved electronic absorption spectra as 6820 cm^{-1} for $Pt(CN)_4^{2-}$[29] and 8600 cm^{-1} for $Ir(CN\text{-}t\text{-}Bu)_4^+$.[30] In both cases the band is assigned to a metal-localized $d_\pi(d_{xz,yz}) \rightarrow \pi^*(p_z)$ transition. The metal–metal-bonded species $Re_2X_8^{2-}$ (X represents halide) was shown to have an ^1E_u–^3E_u separation of about 3000 cm^{-1},[31] though the transition (π(Cl) $\rightarrow$ δ^*) was not metal-localized. For the diruthenium(II,II) system, we would expect the separation to be in the range 7000–8000 cm^{-1} by comparison with those metal-localized transitions of monomeric Pt and Ir complexes. As we shall see below, the spin–orbit perturbation causes a splitting of ca. 1000 cm^{-1}, so there is very little, if any, mixing between the singlet and triplet states. Hence, the magnetic properties of such a complex are mainly determined by the triplet state.

If we write $\phi_1 = \delta^*$, $\phi_2 = \pi_x^*$ and $\phi_3 = \pi_y^*$, then the wavefunctions of ^3E_u are expressed for ^3E_x as

$$\Phi_1 = \|\phi_1^\alpha\phi_2^\alpha\| \qquad M_S = 1 \quad (3a)$$

$$\Phi_2 = \frac{1}{\sqrt{2}}(\|\phi_1^\alpha\phi_2^\beta\| - \|\phi_1^\beta\phi_2^\alpha\|) \qquad M_S = 0 \quad (3b)$$

$$\Phi_3 = \|\phi_1^\beta\phi_2^\beta\| \qquad M_S = -1 \quad (3c)$$

and for ^3E_y as

$$\Phi_4 = \|\phi_1^\alpha\phi_3^\alpha\| \qquad M_S = 1 \quad (3d)$$

$$\Phi_5 = \frac{1}{\sqrt{2}}(\|\phi_1^\alpha\phi_3^\beta\| - \|\phi_1^\beta\phi_3^\alpha\|) \qquad M_S = 0 \quad (3e)$$

$$\Phi_6 = \|\phi_1^\beta\phi_3^\beta\| \qquad M_S = -1 \quad (3f)$$

here "$\|\ \|$" stands for the Slater determinant. When the spin–orbit coupling, $\hat{H}' = \xi \mathbf{L}\cdot\mathbf{S}$, is introduced, the first-order energy matrix can be derived as follows:

$$H' = \begin{pmatrix} 0 & 0 & 0 & \frac{-i\xi}{2} & 0 & 0 \\ 0 & 0 & 0 & 0 & 0 & 0 \\ 0 & 0 & 0 & 0 & 0 & \frac{i\xi}{2} \\ \frac{i\xi}{2} & 0 & 0 & 0 & 0 & 0 \\ 0 & 0 & 0 & 0 & 0 & 0 \\ 0 & 0 & \frac{-i\xi}{2} & 0 & 0 & 0 \end{pmatrix} \quad (4)$$

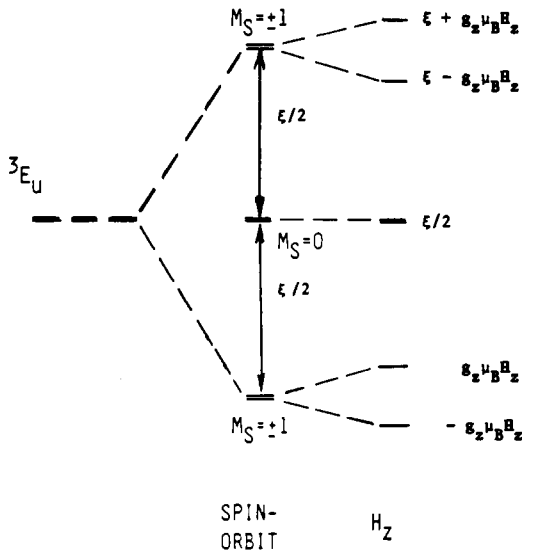

Figure 3. Splitting scheme of ^3E_u under the first-order spin–orbit coupling and the external field H_z.

where ξ is the spin–orbit coupling constant, which is about 1000 cm^{-1} for Ru(II).[32] It is easy to see from this matrix that the coupling occurs only between the states with the same M_S; hence M_S is still a good quantum number under the first-order spin–orbit coupling. Solving the secular determinant $|\lambda I - H'| = 0$, we can find the eigenvalues and eigenfunctions as follows:

$$\lambda_1 = \frac{\xi}{2} \qquad \Psi_1 = \frac{1}{2}(\Phi_1 - i\Phi_4) \qquad M_S = 1 \quad (5a)$$

$$\lambda_2 = 0 \qquad \Psi_2 = \Phi_2 \qquad M_S = 0 \quad (5b)$$

$$\lambda_3 = \frac{\xi}{2} \qquad \Psi_3 = \frac{1}{2}(\Phi_3 - i\Phi_6) \qquad M_S = -1 \quad (5c)$$

$$\lambda_4 = -\frac{\xi}{2} \qquad \Psi_4 = \frac{1}{2}(\Phi_1 + i\Phi_4) \qquad M_S = 1 \quad (5d)$$

$$\lambda_5 = 0 \qquad \Psi_5 = \Phi_5 \qquad M_S = 0 \quad (5e)$$

$$\lambda_6 = -\frac{\xi}{2} \qquad \Psi_6 = \frac{1}{2}(\Phi_3 + i\Phi_6) \qquad M_S = -1 \quad (5f)$$

An energy splitting diagram is shown in Figure 3. From the splitting scheme and the well-known van Vleck equation[33] we can show that the expression for the molar susceptibility (isotropic) is as follows:

$$\chi = \frac{N\mu_B^2 g_{eff}^2}{k_B T} \frac{\cosh u}{1 + \cosh u} \quad (6)$$

where $u = \xi/2k_BT$ and g_{eff} is the effective gyromagnetic ratio. By a simple calculation, it can be shown that at the zero-temperature limit μ_{eff} from the above χ is equal to $\sqrt{3}g_{eff}\mu_B$. Thus the zero-temperature limit is independent of the spin–orbit coupling constant and is in fact the maximum μ_{eff} at any temperature. For comparison, a theoretical curve for the μ_{eff} and the measured μ_{eff} for $Ru_2(fhp)_4(thf)$ were plotted together versus temperature (0–300 K) in Figure 4. It is obvious that this model does not match the measured μ_{eff} curve at all. The $(\pi^*)^3(\delta^*)$ model results in a paramagnetism with weak temperature dependence, while the experimental data indicate that the magnetism should be very temperature-dependent and almost nonmagnetic at the zero-T limit. Hence $(\pi^*)^3(\delta^*)$ cannot be the ground-state configuration for the $Ru_2(xhp)_4$ type molecules or for the $Ru_2(O_2CR)_4$ type.

As we have noted, the possibility of the ^1E_u state lying below ^3E_u is extremely remote. However, even if it did, the behavior

(28) Lever, A. B. P. *Inorganic Electronic Spectra*; Elsevier: Amsterdam, 1984.
(29) Cowman, C. D.; Gray, H. B. *Inorg. Chem.* **1976**, *15*, 2823.
(30) Smith, D. C.; Miskowski, V. M.; Mason, W. R.; Gray, H. B. *J. Am. Chem. Soc.* **1990**, *112*, 3759.
(31) Trogler, W. C.; Cowman, C. D.; Gray, H. B.; Cotton, F. A. *J. Am. Chem. Soc.* **1977**, *99*, 2993.
(32) Abragam, A.; Bleaney, B. *Electron Paramagnetic Resonance of Transition Ions*; Oxford University Press: Oxford, England, 1970.
(33) Ballhausen, C. J. *Molecular Electronic Structures of Transition Metal Complexes*; McGraw-Hill: London, New York, 1979.

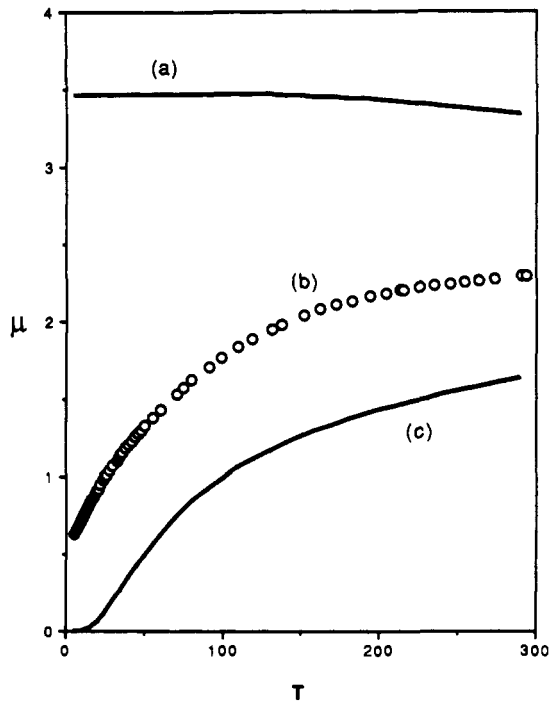

Figure 4. Magnetic moments μ (μ_B) vs T (K), where (a) is calculated from the isotropic susceptibility for ^3E with $g = 2.00$ and $\xi = 1000$ cm^{-1}, (b) gives the measured magnetic moment of $Ru_2(fhp)_4$, and (c) shows the expected behavior of a Boltzmann distribution between a ground state based on a $(\pi^*)^4$ configuration and the ^3E state.

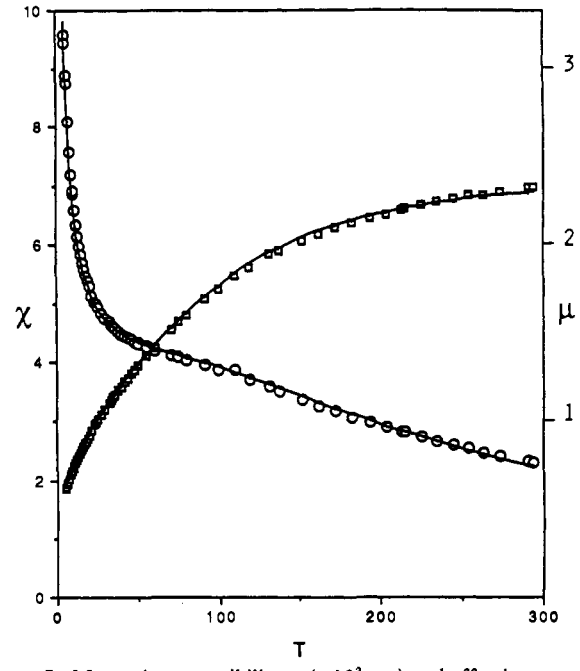

Figure 5. Magnetic susceptibility χ ($\times 10^3$ cgs) and effective magnetic moments μ (μ_B) vs T (K) for $Ru_2(fhp)_4(thf)$, where (O) gives the measured χ and the solid line overlapped with (O) is calculated according to eq 8. The squares and the solid line overlapped with them are the measured and simulated magnetic moments, respectively, with the scale on the right side.

of the system would not be correctly predicted. For a triplet–singlet Boltzmann distribution, the shape of the curve at low temperature is qualitatively different from those measured. The measured μ_{eff} curves approach $T = 0$ asymptotically to the vertical axis, whereas the Boltzmann curve displays an inflection point and approaches $T = 0$ asymptotically to the horizontal axis.

In response to a question raised by a reviewer as to whether the ground state might be an $^1A_1$ state derived from a $(\pi^*)^4$ configuration, with the ^3E state from the $(\pi^*)^3(\delta^*)$ configuration being thermally accessible (a Boltzman distribution), the behavior of such a system has also been calculated for reasonable parameters ($D = 100$ cm^{-1}; $g_{av} = 2.0$). The resulting temperature dependence is also shown in Figure 4. While this curve is in some ways a better model, it fails quantitatively and also shows the wrong qualitative behavior in its approach to the origin.

Now the only hypotheses left is that there is a $(\pi^*)^2(\delta^*)^2$ configuration. As discussed in the carboxylate and previous hydroxypyrimidinate complexes work,[6,14] the magnetic properties of such a system are determined by the zero field splitting (ZFS) of a triplet-ground state term due to second-order spin–orbit coupling. The molar susceptibility for such a system, assuming that the singlet lies lowest, is exactly the same as the well-known axial field model for the mononuclear species[34] and has the following form:

$$\chi_0 = \frac{2N g_{eff}^2 \mu_B^2}{3k_B T} \frac{e^{-x} + \frac{2}{x}(1 - e^{-x})}{1 + 2e^{-x}} \qquad (7)$$

where $x = D/k_BT$. The magnetic susceptibilities of diruthenium tetracarboxylates as well as the three previously known diruthenium hydroxypyridinates were shown to fit the above model very well.[6,14]

The measured molar susceptibilities of $Ru_2(fhp)_4(thf)$, like those of the other hydroxypyridinate complexes, can be expressed as[14]

$$\chi_M = (1 - \alpha)\chi_0 + \alpha\chi_{imp} \qquad (8)$$

where χ_0, the contribution from the pure diruthenium(II,II) complex, is defined in eq 7. χ_{imp} is incorporated to explain the weak paramagnetism in the low temperature region due to small amount of oxidized impurity, and α is the molar fraction of impurity. As reasoned before, the measured susceptibilities for $Ru_2(butyrate)_4Cl$[35] were used as χ_{imp}. By a nonlinear least-squares fitting to eq 8, the values of α, D, and g_{eff} were calculated to be 0.024, 263 (4) cm^{-1}, and 1.64 (1), respectively, which are essentially in the same range as those determined for other hydroxypyridinate complexes. The simulated curves for both the susceptibility and the effective magnetic moment are also plotted in Figure 5. It is obvious from the plot that the measured data overlap the model curves very well. Hence the magnetic behavior of $Ru_2(fhp)_4(thf)$ is in full accord with the $(\pi^*)^2(\delta^*)^2$ configuration. So far we have seen that all the diruthenium hydroxypyridinate complexes consistently adopt this configuration. This consistency reveals the interesting fact that the local inequivalence of the two metal atoms in the diruthenium core does not affect the global electronic structures.

SCF-Xα calculations were performed on the model molecules in order to obtain more quantitative information about the molecular electronic structures. Although $M_2(xhp)_4$ type molecules are very common, there is no published MO study on this class of compounds as yet. The calculations performed were simplified by utilizing the $HNC(H)O^-$ fragment as a substitute for the xhp^- anion. Among four possible coordination modes (Figure 2) only the two extreme situations, the most symmetrical one D_{2d} and the most polar one C_{4v}, were considered. The other two, C_{2h} and C_s should not differ very much, and they can be viewed as intermediates. In the C_{4v} model, the OH^- anion was used both to mimic the axial coordination of THF and to preserve the symmetry. Since the oxygen atom in OH^- is fixed at the actual position of the oxygen in THF, the negative charge should not affect the electronic structure greatly. H_2O would be better as a model for the THF ligand, but the 4-fold symmetry would be destroyed, and this would complicate the computation.

Since we are concentrating on the metal–metal antibonding orbitals that are influenced by the lone pairs of ligands, the low energy and ligand-localized orbitals are ignored in further dis-

(34) Carlin, R. L. *Magnetochemistry*; Springer-Verlag: Berlin, 1986.

(35) Telser, J.; Drago, R. S. *Inorg. Chem.* **1984**, *23*, 3114.

Table III. Upper Valence Molecular Orbitals for $Ru_2(HNC(H)O)_4$ (D_{2d})[a]

level	E, eV	% charge Ru	O	N	C	H_C	H_N	Ru angular contribution
$8b_2$	−4.458	89	7	3	0	0	1	2% s, 8% p, 90% d
$3a_2$	−5.903	70	11	18	1	0	0	100% d
11e	−6.039	97	1	1	1	0	0	100% d
$3b_1$	−7.074	64	2	23	11	0	0	100% d
$2b_1$	−7.933	29	37	34	0	0	0	100% d
10e	−7.994	2	26	67	5	0	0	
9e	−8.458	49	23	20	2	4	2	4% p, 96% d
8e	−9.165	54	11	23	7	5	0	8% p, 92% d
$8a_1$	−9.234	59	20	12	4	5	0	34% s, 4% p, 61% d
$2a_2$	−9.302	34	1	55	10	0	0	100% d
7e	−9.689	6	52	36	1	0	5	
$7b_2$	−10.610	22	63	6	4	4	1	8% s, 1% p, 91% d
$7a_1$	−10.801	52	38	4	3	3	0	1% p, 98% d
$1a_2$	−11.336	6	76	2	16	0	0	
6e	−11.516	1	67	11	21	0	0	
$6b_2$	−11.532	33	3	46	6	6	6	11% s, 89% d
$6a_1$	−11.744	36	10	39	4	3	7	3% s, 1% p, 97% d

[a] % charge indicates relative amount of charge in the atomic spheres, and metal angular contribution is given only when >10%. The gap is between the HOMO and the LUMO.

Table IV. Upper Valence Molecular Orbitals for $Ru_2(HNC(H)O)_4$ (C_{4v})[a]

level	E, eV	% charge Ru_O	Ru_N	O	N	C	H_C	H_N	Ru_O angular contribution	Ru_N angular contribution
$9a_1$	−4.798	46	43	6	4	0	0	1	2% s, 6% p, 92% d	3% s, 7% p, 90% d
$4b_2$	−6.234	32	39	13	16	1	0	0	100% d	100% d
11e	−6.436	54	42	2	1	1	0	0	100% d	100% d
$3b_2$	−7.499	56	30	2	3	10	0	0	100% d	100% d
$2a_2$	−7.857	0	0	26	69	5	0	0		
10e	−8.272	1	0	22	71	5	1	0		
9e	−8.678	23	41	21	11	1	2	1	2% p, 98% d	2% p, 98% d
$8a_1$	−9.424	30	35	18	9	3	5	0	33% s, 5% p, 62% d	28 %s, 3% p, 69% d
8e	−9.476	23	18	29	15	6	8	0	9% p, 91% d	12% p, 88% d
7e	−10.057	1	4	38	48	1	0	7		
$2b_2$	−10.062	6	35	16	42	1	0	0		100% d
$7a_1$	−10.881	32	9	48	5	2	3	1	1% s, 99% d	
$7b_1$	−10.922	24	2	56	7	5	6	0	100% d	

[a] % charge indicates relative amount of charge in the atomic spheres, and metal angular contribution is given only when >10%. The gap is between the HOMO and the LUMO.

cussion. For the D_{2d} model, the energy levels, relative populations, and angular distribution of the ruthenium contribution for 17 upper valence orbitals are listed in the Table III, while all localized C–O, C–N, C–H, and N–H σ-bond orbitals and four ligand-delocalized π-bond orbitals are omitted. On the basis of the relative charge contributions, the metal–metal bonding and antibonding orbitals can be identified as (in descending energy order) $8b_2$ (σ^*), $3a_2$ (δ^*, LUMO), 11e (π^*, HOMO), $3b_1$ (δ), 9e and 8e (π plus Ru–O and Ru–N), and $8a_1$ and $7a_1$ (σ plus Ru–O and Ru–N). There are appreciable ligand contributions in all of the metal–metal bonding orbitals as shown by the data in Table III. In contrast, ligand contributions become minor in the metal–metal antibonding orbitals, especially in π^* (11e). An important result of this calculation is that the δ^*–π^* (LUMO–HOMO) separation is only 0.14 eV, while the π^*–δ (HOMO–SHOMO) separation is much larger, 1.03 eV. This is in full accord with our qualitative discussion, given above, that δ^* and π^* levels are very close (pseudodegenerate), although it is not an unequivocal result due to the limitations of the Xα method. A contour plot of the δ^* orbital ($3a_2$) (Figure 6) clearly shows the antibonding contribution from the lone-pair orbital of the ligand. The contribution from the nitrogen atoms to the δ^* orbital (18%) is larger than that of the oxygen atoms (11%), which is not quite consistent with our previous qualitative comment that oxygen should have the dominant contribution.[14] This is probably due to the fact that the model fragment we chose, $HNC(H)O^-$, more closely resembles the amido ligand than the hydroxypyridinate ligand. It is well-known that the amide is less acidic than the 2-pyridinol. Hence the nitrogen atom in the model is more basic (less electronegative) than that in the real complex, which results in a larger δ^*–π^* gap.

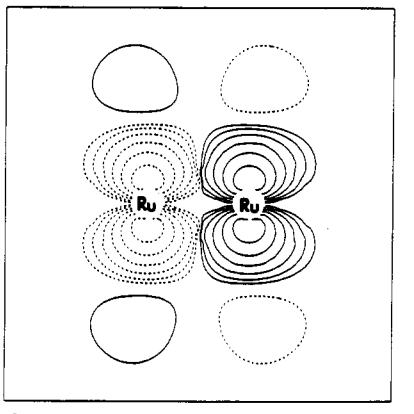

Figure 6. δ^* of $Ru_2(HNC(H)O)_4$ (D_{2d}). The projection plane bisects the xz and yz planes.

An SCF–Xα calculation with a $C_5H_4NO^-$ ligand would give a more accurate description of the molecular electronic structures, but we have not succeeded in doing so due to the difficulty of the calculation.

The results of converged SCF calculations for C_{4v} models without and with the axial OH^- are listed in Tables IV and V, respectively. Like the D_{2d} case just discussed, all of the ligand σ-bonding orbitals and several lowest ligand π-bonding orbitals are omitted. The relative energy levels and charge distributions of the metal–metal bonding and antibonding orbitals in both model calculations are also essentially the same as those found in the D_{2d} case. The metal–metal bonding (antibonding) orbitals are

Table V. Upper Valence Molecular Orbitals for $Ru_2(HNC(H)O)_4(OH)^-$ (C_{4v})[a]

		% charge									Ru$_O$ angular contribution	Ru$_N$ angular contribution
level	E, eV	Ru$_O$	Ru$_N$	O	O$_t$	N	C	H$_C$	H$_N$	H$_t$		
11a$_1$	−0.558	49	36	7	3	3	0	0	1	1	1% p, 99% d	2% s, 11% p, 87% d
4b$_2$	−2.423	20	49	12	0	17	2	0	0	0	100% d	100% d
12e	−2.564	44	38	1	15	1	1	0	0	0	100% d	100% d
11e	−3.595	2	22	2	73	1	0	0	0	0		
3b$_2$	−3.894	64	22	5	0	1	9	0	0	0	100% d	100% d
2a$_2$	−3.920	0	0	27	0	68	5	0	0	0		
10e	−4.366	0	1	24	1	69	5	0	0	0		
9e	−4.874	19	22	37	2	13	2	4	1	0	63% p, 94% d	5% p, 95% d
10a$_1$	−5.175	25	40	9	11	7	2	3	0	3	22% s, 14% p, 64% d	23% s, 2% p, 75% d
8e	−5.712	38	21	21	2	8	5	5	0	0	4% p, 96% d	6% p, 94% d
7e	−6.143	1	5	32	0	53	2	0	7	0		
2b$_2$	−6.189	9	33	15	0	42	2	0	0	0		
9a$_1$	−6.595	14	2	53	14	5	3	4	0	4	24% s, 1% p, 75% d	
7b$_1$	−7.046	26	2	55	0	7	5	5	0	0	100% d	
1a$_2$	−7.289	0	0	66	0	10	24	0	0	0		
6e	−7.747	1	0	64	0	12	23	0	0	0		
8a$_1$	−7.890	1	23	9	5	44	5	4	8	1		
6b$_1$	−8.217	0	35	7	0	40	6	5	7	0		
7a$_1$	−8.321	23	10	1	48	2	1	1	0	13	5% s, 95% d	1% s, 5% p, 94% d

[a] % charge indicates relative amount of charge in the atomic spheres, and metal angular contribution is given only when >10%. 12e is half-occupied (see text). The gap is between the HOMO and LUMO.

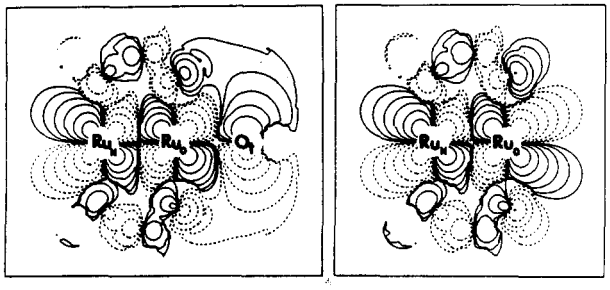

Figure 7. π^* of $Ru_2(HNC(H)O)_4$ (C_{4v}) with (left) and without (right) OH^-. The projection plane is the xz plane.

(in descending energy order) for the model without axial OH^-, 9a$_1$ (σ^*), 4b$_2$ (δ^*, LUMO), 11e (π^*, HOMO), 3b$_2$ (δ), 9e and 8e (π plus some metal–ligand π bond), and 8a$_1$ (σ), and for the model with axial OH^-, 11a$_1$ (σ^*, LUMO), 4b$_2$ (δ^*, HOMO), 12e (π^*), 3b$_2$ (δ), 9e and 8e (π plus some metal–ligand π bond), and 10a$_1$ (σ). The extra upper valence orbitals introduced by adding axial OH^- are 11e (mainly the lone pairs of axial oxygen) and 7a$_1$ (Ru–O$_t$ σ bond).

When there is no axial interaction, the δ^* orbital lies about 0.2 eV above the π^* orbital. From Table IV it is obvious that electron density is more concentrated on the Ru$_O$ atom, due to the electron-withdrawing ability of oxygen. However, this local difference does not alter the overall global electronic structure, which is consistent with the fact that all $Ru_2(xhp)_4$ compounds have similar magnetic behavior even though there are three different coordination modes. When the OH^- is added to the axial position, not only does the δ^* (4b$_2$)–π^* (12e) separation decrease by 0.06 eV to 0.14 eV but the calculation also converges to a different configuration, namely, $(\pi^*)^2(\delta^*)^2$. This is due to the destabilizing effect of the axial ligand with a π type lone pair, which predominantly interacts with the π^* orbital of the metal core. This interaction is also reflected in the contribution of the axial oxygen atom to the π^* orbital (14%). The contour plots of π^* for the C_{4v} model both with and without OH^- (Figure 7) clearly show the influence of this antibonding combination.

The results of the present SCF–Xα calculations have consistently shown that there exists a small δ^*–π^* gap for $Ru_2(xhp)_4$ complexes and thus favor the $(\pi^*)^2(\delta^*)^2$ ground-state configuration. However, it is well to remember that very subtle features of the electronic structures are beyond the capability of Xα method. It is interesting to note that Norman et al. suggested a $(\pi^*)^3(\delta^*)$ ground-state configuration for $Ru_2(O_2CH)_4$ on the basis of the small δ^*–π^* gap found in their by Xα calculation.[8] However a recent ab initio restricted Hartree–Fock (RHF) calculation on this model showed that $(\pi^*)^2(\delta^*)^2$ was the correct ground-state configuration by the total energy criterion.[10] It is hoped that the work in this laboratory employing a combination of supercomputer and SCF calculations including CI will completely resolve this problem in the near future.

Acknowledgment. We thank the National Science Foundation for support. We thank Professor J. L. Dye of Michigan State University for making his facility available for the measurement of the susceptibility data and Dr. X. Feng of this laboratory for the helpful discussions.

Supplementary Material Available: Complete tables of crystal data, positional parameters, bond distances and angles, and anisotropic displacement parameters and a table of magnetic susceptibility data (9 pages); a table of observed and calculated structure factors (11 pages). Ordering information is given on any current masthead page.